Topologically Protected Exceptional Point with Local Non-Hermitian Modulation in an Acoustic Crystal

Zhongming Gu,[1,2] He Gao,[1,2] Tuo Liu,[1,2] Shanjun Liang,[1,2] Shuowei An,[1] Yong Li,[3,*] and Jie Zhu[1,2,†]

[1] *Research Center for Fluid-Structure Interactions, Department of Mechanical Engineering, The Hong Kong Polytechnic University, Hung Hom, Kowloon, Hong Kong SAR, People's Republic of China*

[2] *The Hong Kong Polytechnic University Shenzhen Research Institute, Shenzhen 518057, People's Republic of China*

[3] *Institute of Acoustics, Tongji University, Shanghai 200092, People's Republic of China*

(Received 11 August 2020; revised 3 November 2020; accepted 14 December 2020; published 14 January 2021)

The topological edge state (TES) may emerge at the interface between acoustic crystals with distinct topological properties. It supports robust wave phenomena against geometry imperfections. By imposing holistic onsite gains and losses in *PT* symmetric Su-Schrieffer-Heeger lattices, zero mode can be obtained from the convergence of two splitting TES modes induced by adjacent coupling. However, the nonlocal non-Hermiticity requires exorbitant configuration on each atom, resulting in complex systems. Here, we demonstrate the effect of local non-Hermitian modulation to the coupled TESs, utilizing passive acoustic crystals with sandwiched arrangements. Local non-Hermiticity is introduced at the position of one of the TESs to manipulate the splitting TESs. By suitably adjusting the non-Hermitian strength, the splitting TESs experience the coalescence process along with the asymmetric reflection and absorption near and beyond the exceptional point. Due to the topological essentials, the emergence of the exceptional point also can be proved to be robust to the geometrical disorders. Our results reveal that coupled TESs can be modulated by local non-Hermiticity to realize the extraordinary scattering phenomena, which may inspire more acoustic functional devices based on the topological or non-Hermitian characteristics.

DOI: 10.1103/PhysRevApplied.15.014025

I. INTRODUCTION

The recent discovery of topological insulators (TIs) has attracted ongoing interests due to the intriguing physics property of behaving as an insulator in the interior while supporting robust metallic states at the surface [1]. With topological transition from trivial phase to nontrivial phase, TI gives rise to many exotic states of matters, such as quantum spin Hall effect [2], topological semimetal [3], dissipationless transport [4], etc. Due to the similar topological band theory, this concept was also extended to classical wave systems, from electronics to photonics, phononics and mechanics, inspiring various robust wave transport realizations [5–9]. Among them, the acoustic system has been regarded as an excellent platform to exemplify the universality and diversity of the topological phase as it has macroscopic dimensions for convenient fabrication and flexible observation [10]. Experimental demonstrations have been conducted to verify the hallmarks of topological notion in acoustics, like multipole topological insulators [11–13], topological valley transport [14], high-order topological states [15,16]. Remarkable functionalities based on these interesting properties have also been proposed, like robust analog signal processing [17,18], negative refraction [19], and delay lines [20].

On the other hand, the concept of *PT* symmetry and non-Hermitian physics has also been introduced to classical wave systems recently [21–25]. At the critical point that links the exact *PT* symmetry and the broken *PT* symmetry, also known as the exceptional point (EP), the system exhibits extraordinary scattering phenomena, which are guaranteed by the generalized energy conservation in the open environment [26–31]. In particular, by solely incorporating the loss, a well-designed structure can still preserve the signature of EP and lead to the asymmetric wave manipulation [32–36]. Meanwhile, many efforts have been devoted to studying the non-Hermitian characteristics of the TIs. With the help of non-Hermiticity, unexpected freedom to manipulate the system topology appears and gives rise to beam steering, high-order topological corner states and flat bands [37–41]. Recently, the breakup of zero mode has been demonstrated to be recovered by the well-engineered global loss distribution in

*yongli@tongji.edu.cn
†jiezhu@polyu.edu.hk

photonics [42]. However, the global onsite loss and gain modulations imposed on each atom inevitably give rise to the complexity of system and lower the flexibility.

In this work, we present a study on the non-Hermitian characteristics of one-dimensional heterogeneous acoustic crystal, where two end parts sandwich a middle part with different topological properties. Due to the transition of Zak phase in the bulk band, topological edge state (TES) emerges at the interfaces between different parts [43]. If the middle part has a finite size, the TESs at two interfaces may interact with each other, leading to the zero-mode splitting in the real spectrum. It can also be observed from the transmission spectrum that there appear to be two peaks within the overlapped bandgap of the two different kinds of acoustic crystals, as shown in Fig. 8 in Appendix A. By introducing suitable dissipation, for example, adding sound-absorbing materials (SAMs) at the position of either interfaces, the interaction can be compensated. The splitting can be recovered and the modes coalesce again in the real spectrum. Increasing dissipative loss, the system crosses the EP and works in the *PT*-broken phase, associated with the asymmetric reflections. Unlike the conventional non-Hermitian lattice, which needs the periodically nonlocal on-site modulation [14,38], our proposed model extremely simplifies the design that only needs local non-Hermitian modulation at the position of TESs, and may find potential applications in acoustic sensing, filtering, and imaging.

II. MODEL AND ANALYSIS

As shown in Fig. 1, the acoustic crystal consists of periodically arranged rigid rods with Neumann boundary condition inside a waveguide with a square cross section of l^2, where $l = 50$ mm. The acoustic crystal's unit cell contains two rigid rods with a lattice constant of $2D = 180$ mm, and each rod has the radius $R = 14$ mm. Tuning the distance d between the two rods of a unit cell can close and reopen the bandgap, which means the system undergoes a topological transition due to the band inverters and changes the topological properties of the bandgap. The acoustic crystal is accordingly designed to have three different parts. The two parts at two ends are labeled as S1 with rods painted blue. They have the same structure parameter $d_1 = 130$ mm. The part in the middle, labeled as S2 with rods painted yellow, has a different structure parameter $d_2 = 150$ mm. The topological edge states emerge at the interfaces between S1 and S2 are labeled as TES1 and TES2, respectively. Apparently, we can modulate the coupling strength between the TES1 and TES2 by changing the number of unit cells in S2. When the length of S2 is much smaller than the coupling limit length, the coupling effect cannot be neglected. A strong interaction between the two TESs leads to the large splitting in the real spectrum. In contrast, when the length is beyond the coupling limit, the interaction vanishes and the zero-mode remains intact.

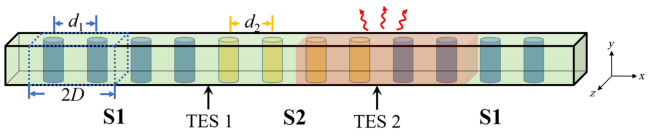

FIG. 1. The studied one-dimensional heterogeneous acoustic crystal waveguide. Each unit cell contains two rigid rods with a lattice constant of $2D$. At two ends, S1 (blue rods) represents the part with distance between two rods inside a unit cell being d_1. S2 (yellow rods) in the middle has a different distance d_2. TES 1 and TES 2 represent the topological edge states at the interface between S1 and S2. Sound dissipation is intentionally introduced at the position of TES 2 to study the effect of non-Hermitian modulation.

Firstly, we study the band structures of S1 and S2, as shown in Figs. 2(a) and 2(b), respectively. The eigenmode analysis is conducted with finite-element-method simulation (COMSOL Multiphysics). The mass density and sound speed of the background medium are set as $\rho_0 = 1.21$ kg/m^3 and $c_0 = 343$ m/s. The second bandgap of each structure has been painted in green and blue, respectively. The topological properties of the bandgaps can be described by the summation of the Zak phase of each band below it [43]. For the unit cell protected by mirror symmetry with respect to the central cross section, the Zak phase can only have two values: 0 and π, which can be obtained from the symmetry properties of the band-edge states [7]. If the states at the center and edge have the same symmetry with respect to the central cross section, no matter whether it is even or odd, the Zak phase of this band is 0. Otherwise, the Zak phase is π. By accumulating the Zak phase of each band, as marked in red in Figs. 2(a) and 2(b), the second bandgaps of S1 and S2 are proved to have different topological properties. Figure 2(c) shows the evolutions of the central states of the second and third bands as a function of the distance between the two rods, which can indicate that the band inverts.

As we mention above, in the Hermitian case, the coupled TESs can be modulated by the length of S2. Figure 3 shows the coupled TESs in the real and imaginary spectra, in which N denotes the number of S2units S2. During the simulation, each S1 part at the end contains three units. Obviously, fewer S2 units leads to stronger coupling between the TESs, which is proved in Fig. 3(a). With increasing N, the splitting modes emerge again gradually as expected. Meanwhile, Fig. 3(b) shows that the imaginary part of the eigenfrequency remains almost unchanged with low values since only radiation loss is considered in the Hermitian case.

Next, let us consider adding a non-Hermitian modulation to the vicinity of TES2 with $N = 3$. The lossy domain

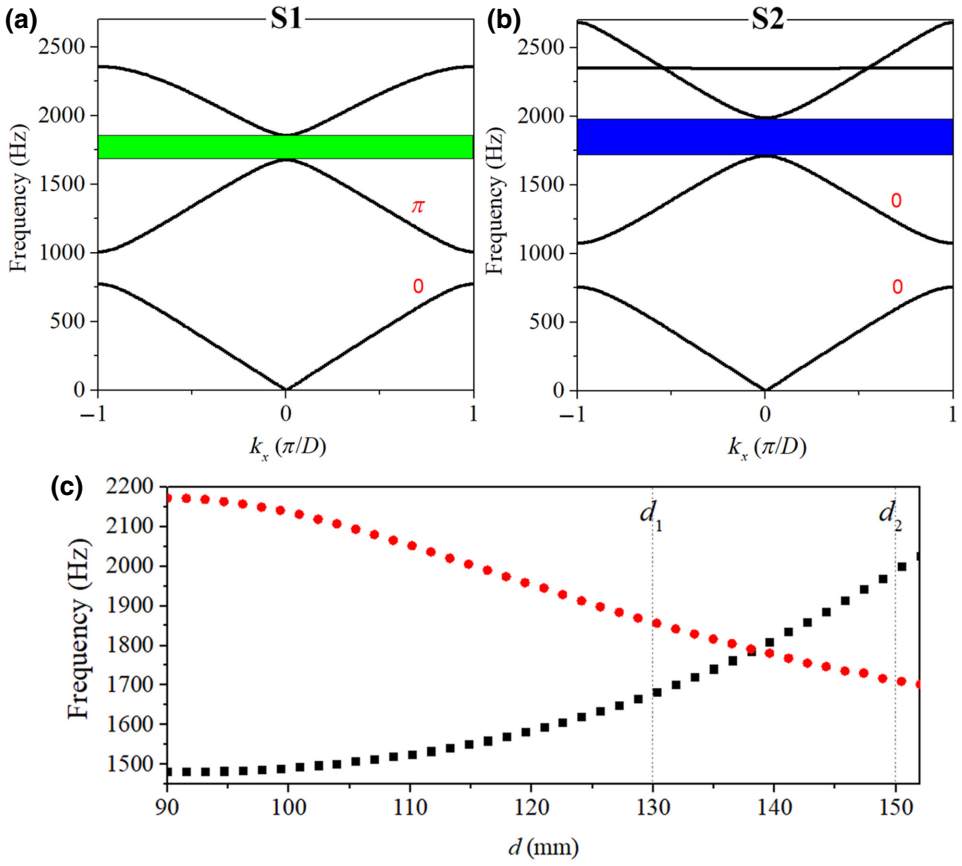

FIG. 2. Band structures of S1 (a) and S2 (b), respectively. The second bandgap is painted in green and blue. The Zak phase of each band below the second bandgap is marked in red. (c) The central state of the second and third bands as a function of the distance d. The red dot indicates the odd mode and the black square indicates the even mode (with respect to the central cross section of the units).

has two units as depicted by the red region in Fig. 1. It is tuned to induce the broken PT symmetry. For the lossy domain, the mass density and sound speed have been set as $\rho_L = \rho_0$ and $c_L = c_0(1 + i\delta)$ to introduce the non-Hermitian modulation. As what we study is a narrow-band phenomenon, we can use this constant expression to represent the loss. The real and imaginary eigenmodes' spectra when there is non-Hermiticity are shown in Figs. 4(a) and 4(b), respectively. Within the overlapped bandgap shared by S1 and S2, the newly created modes have a clear response to the increased non-Hermitian strength. After the EP at $\delta = 0.059$, the two eigenmodes generated by the topological properties of the system coalesce in the real spectrum while bifurcating to two branches in the imaginary spectrum: "less lossy" mode and "more lossy" mode. We also examine the according eigenmodes around the EP. The sound energy fields corresponding to the four eigenmodes marked in Fig. 4(a) are shown in Fig. 4(c). It is obvious that, before the EP, the eigenmodes still preserve the profiles of confined states at the two interfaces. In this regime, also known as the PT-exact phase regime, the energy of eigenmodes are distributed symmetrically. However, beyond the EP, the eigenmodes drastically change as the system becomes PT broken. In this regime, the symmetrical characteristics of the eigenmodes are broken. They reside in either the "less lossy" or "more lossy" modes.

For a comparison, the process can also be described by the coupled mode theory [44]:

$$\frac{da_1}{dt} = -i\omega_1 a_1 + i\kappa_{12} a_2, \tag{1}$$

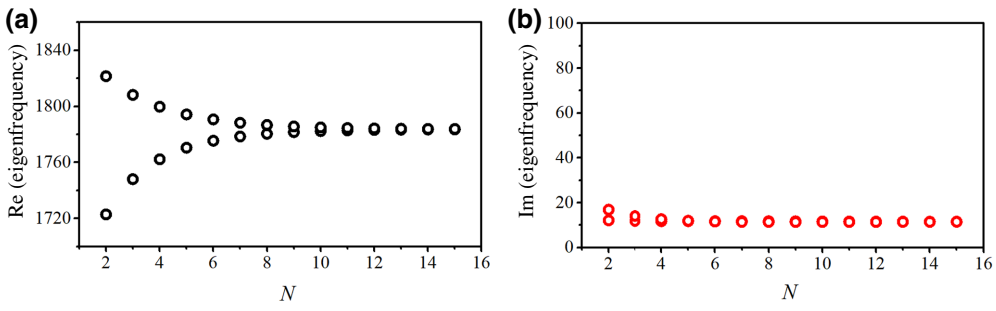

FIG. 3. The real part (a) and the imaginary part (b) of the eigenvalues of the splitting modes with different N in the Hermitian case.

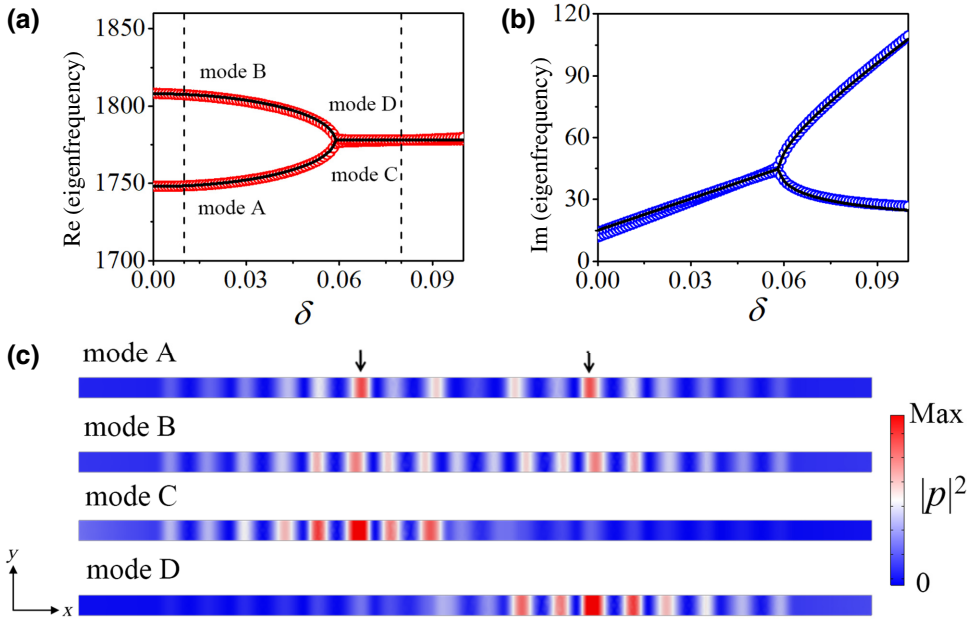

FIG. 4. (a) The real-part evolution of the eigenmode in the presence of changing non-Hermitian loss modulation. (b) The imaginary-part evolution of the eigenmode. The black solid lines represent the analytical results based on the coupled mode theory. (c) Sound energy distributions associated with the four eigenmodes marked in (a).

$$\frac{da_2}{dt} = -i\omega_2 a_2 + \gamma a_2 + i\kappa_{21} a_1, \tag{2}$$

where a_1 and a_2 denote the complex amplitude of the field in the coupled TESs, respectively. ω_1 and ω_2 represent the eigenfrequency of the states. κ_{12} and κ_{21} are the coupling strength, γ is the loss coefficient at the TES2, but has a different dimension with δ. The relation between γ and δ can be determined by fitting the position of EP in the parameter space. As protected by the structural symmetry, we can let $\omega_1 = \omega_2 \equiv \omega_0$ and $\kappa_{12} = \kappa_{21} \equiv \kappa$. Then by solving the eigenvalues of the coupled mode equations, the according eigenfrequencies can be expressed as

$$\omega_\pm = \omega_0 + \frac{i\gamma}{2} \pm \sqrt{\kappa^2 - \frac{\gamma^2}{4}}. \tag{3}$$

In the Hermitian case with $\gamma = 0$, Eq. (3) will be degenerated to $\omega_\pm = \omega_0 \pm \kappa$, which describes the splitting of the eigenmodes. However, with increasing γ, the eigenmodes will recover and merge gradually in the real spectrum, while the imaginary part will arise at the same time. Beyond the EP, where $\kappa^2 - \gamma^2/4 = 0$, the system will work in the broken *PT* phase with merged real parts and bifurcated imaginary parts. With the initial values retrieved from the simulation in Hermitian cases ω_0 = 1779 Hz and κ = 30 Hz, the analytical results have been plotted in Figs. 4(a) and 4(b) with black solid lines. In the imaginary part, we add an overall bias γ_0 = 15 Hz to represent the radiation loss.

III. TRANSMISSION PROPERTIES AROUND THE EP

To evidently demonstrate the mode evolution, the scattering properties are calculated in the $f - \delta$ parameter space and displayed in Fig. 5. We define $r_{L(R)}$ and $t_{L(R)}$ as the reflection and transmission coefficients of the two-port waveguide. The subscripts L and R represent the left- and right-side incidence, respectively. Without non-Hermitian modulation, the transmission properties along both directions should be identical due to the reciprocity principle. However, as the lossy effect is imposed at the position of TES2, the space symmetry is broken. The reflections for incidences from both sides become dramatic different. As shown in Fig. 5(a), for the left-side incidence, two reflection dips at $\delta = 0$ that corresponds to the two TESs gradually merge into one dip around $\delta = 0.059$ and beyond. Counterintuitively, the two reflection dips gradually vanish where high reflection emerges as δ increases for the right-side incidence, as shown in Fig. 5(b). Since the system undergoes transition from *PT*-exact phase to *PT*-broken phase, sound incident from the left-side excites the "more lossy" mode. Most energy is absorbed within a broad range of non-Hermitian modulation. In contrast, sound incident from the right-side excites the "less loss" mode. Most energy gets reflected owing to the acoustic crystal's scattering characteristic. The asymmetric properties around the EP can also be observed in the reflection phase diagram. As shown in Figs. 5(c) and 5(d), with $\delta = 0$, both left- and right-side incidences have two phase discontinuities caused by the topological transitions at the splitting modes. However, beyond the EP, reflection phase for the left-side incidence just has one phase shift, which is the product of broken *PT* symmetry. On the other hand, reflection

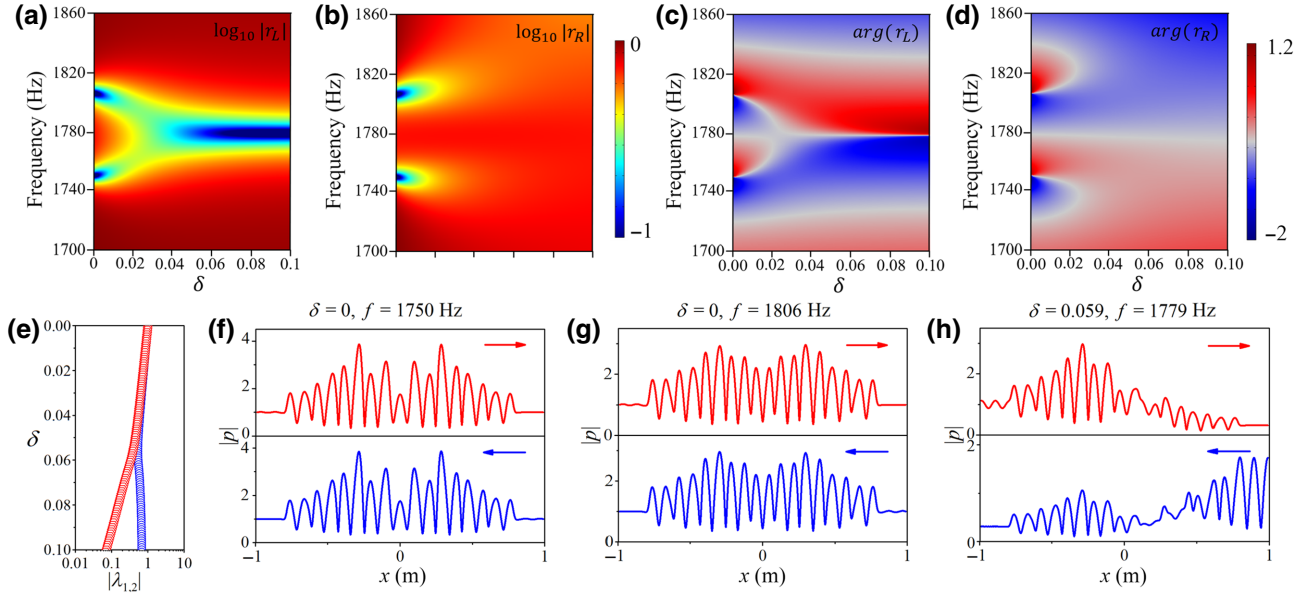

FIG. 5. The simulated scattering properties. (a) The logarithm of reflection for left-side incidence. (b) The logarithm of reflection for right-side incidence. (c) The phase of reflection for left-side incidence. (d) The phase of reflection for right-side incidence. (e) The eigenvalues retrieved from the scattering matrix as a function of δ. (f)–(h) The intensity distributions along the waveguide for $\delta = 0$, $f = 1750$ Hz, $\delta = 0$, $f = 1806$ Hz, and $\delta = 0.059$, $f = 1779$ Hz. Left-side incidences are marked in red while the right-side incidences are marked in blue.

phase for the right incidence gradually grows to be smooth and continuous in the parameter space with stronger non-Hermitian modulation. Retrieving the reflections and transmission information from the simulations, we can calculate the eigenvalues of the scattering matrix $S = \begin{pmatrix} r_L & t \\ t & r_R \end{pmatrix}$. It can closely describe the phenomena of spontaneous PT-symmetry breaking and is consistent with the mode analysis. Consequently, the eigenvalues of S can be expressed as $\lambda_{1,2} = \left(r_L + r_R \pm \sqrt{(r_L - r_R)^2 + 4t^2}\right)/2$. The eigenvalue's amplitude change with δ at $f = 1779$ Hz is calculated and shown in Fig. 5(e). Different from the cases of balanced gain and loss where the eigenvalues always preserve reciprocal amplitudes [29], in the passive system, the eigenvalues of S overlap in the exact PT symmetry phase, degenerate at the EP around $\delta = 0.059$, then diverge in the broken PT symmetry phase, which perfectly follows the coupled mode analysis. These asymmetric scattering responses can be utilized for filtering acoustic signals, which can also be adjusted with the non-Hermitian modulation.

The spatial profiles depicted in Figs. 5(f) and 5(g) clearly show distinct intensity distribution at the resonant frequencies in the process of mode coalescence. When $\delta = 0$, the PT symmetry is preserved, the intensity profile remains spatially symmetric. Incidences from both sides have the identical distributions at the splitting TES frequencies 1750 and 1806 Hz. Sound energy is highly confined at the two TESs. However, approaching the EP, the coupled modes gradually merge into one resonant mode at 1779 Hz. The spatial symmetry of intensity profile is gone. For left-side incidence, the TES1 still survives despite the presence of the lossy domain. It is associated with the more lossy mode. However, for right-side incidence, most energy is reflected, coinciding with the less lossy mode.

We conduct experiments to measure the fabricated sample with different non-Hermitian loss modulations. The experiment setup is shown in Fig. 6(a). Four microphones are utilized to measure the scattering information. Sliced SAMs are placed in the waveguide to introduce different magnitude of loss. By exchanging the positions of SAM at either TESs, we can mimic the cases for left- and right-side incidences effectively. The amplitudes of reflections are shown in Fig. 6(b). When $\delta = 0$, the sound reflections for both side incidences are almost the same. Two dips induced by the interplays of TESs can be observed. If SAM is added to introduce weak loss, the reflection profiles for left-side (red line) and right-side incidence (blue line) start to separate but still possess the similar two dips. It is consistent with the simulation results shown in Figs. 5(a)–5(d). The introduced loss effect is too small to compensate the coupling strength. When more slices of SAM are added so that the loss effect is strong enough to surpass the EP, dramatic different reflections can be observed as the system transmits to the PT-broken phase, consistent with the theoretical analysis. For left-side incidence, the reflection approaches minimum at 1796 Hz with a broad dip. While the reflection remains high without much variation over

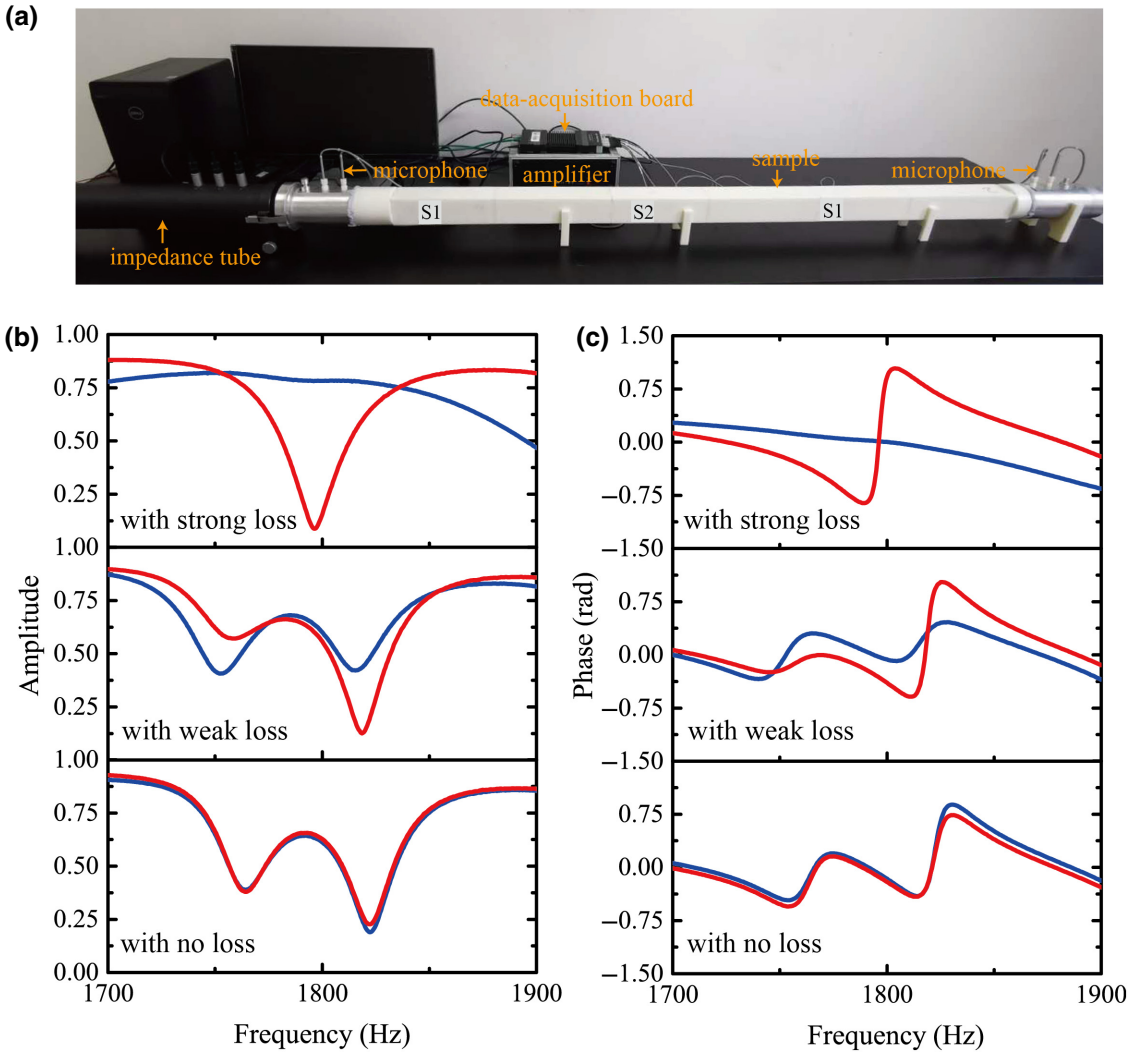

FIG. 6. Measured reflections change with frequency for different non-Hermitian loss modulations. (a) The experiment setup. (b) The change of amplitude for the three cases of no loss, weak loss, and strong loss. (c) The change of phase. The red and blue lines represent the left and right incidences, respectively.

the spectrum for right incidence. The measured 1796 Hz is slightly different from the calculated 1779 Hz because the introduction of SAM also changes the resonant frequency. Figure 6(c) shows the reflection's phase response to the non-Hermitian modulation. When there is no loss modulation, or the loss is too weak to induce the EP, there are two visible variations. However, when the loss surpasses the critical value, the phase response changes smoothly for right incidence while still with an obvious shift for left incidence.

IV. ROBUSTNESS TO THE DISORDERS

To reveal the unusual characteristics of the coupled TESs with the non-Hermitian modulation, we further study the robustness of EP subject to geometric imperfections such as position disorders and radii deformations. In fact, as long as the topological properties are preserved, TESs can still be excited at the interface between parts with different topological phases. It is highly possible that imperfections will change the coupling strength, but adjusting the loss modulation accordingly can still make the system working in the vicinity of the EP. We firstly impose a position deviation on each rod to introduce position disorder. As shown in Fig. 7(a), R' indicates the value of position deviation and θ is the deviation angle, which is generated randomly. Under this circumstance, the coupled TESs still can be excited due to the different topological properties. The two dark bands in Fig. 7(b) clearly indicate that the coupled edge modes are stable even when R' reaches up to 10% of the rod's radius. Therefore, the non-Hermitian degeneracy of the coupled TESs as a function of the loss modulation can still be observed, as depicted in Fig. 7(c).

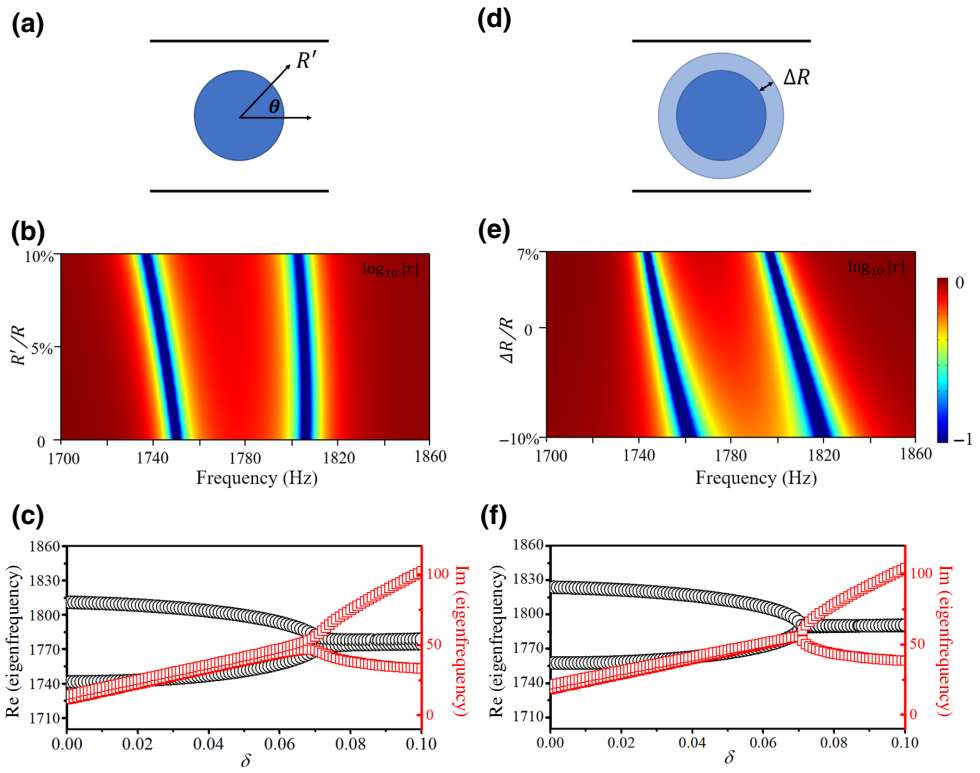

FIG. 7. Effects of geometry imperfections on the emergence of EP. (a) The model of position disorder imposed to the rods. (b) The logarithmic of reflection spectrum as a function of R' when there is no non-Hermitian loss modulation. (c) The emergence of EP in the presence of varying loss modulations for the case of $R' = 10\%R$. (d) The model of radii deformation imposed to the rods. (e) The logarithmic of reflection spectrum as a function of ΔR when there is no non-Hermitian loss modulation. (d) The emergence of EP in the presence of varying loss modulation with $\Delta R = -10\%R$.

The effects of radii deformation, as shown in Fig. 7(d), are investigated by sweeping the offset of the radius, ΔR. It is done from -10% to 7% of the rod's radius so collisions between the rods can be avoided. We apply the same radii deformations to all rods to prevent from breaking the chiral symmetry. Similar to the position disorder case, two dark reflection bands can be observed, and the emergence of EP can still be obtained with appropriate non-Hermitian modulation. The results demonstrated in Figs. 7(e) and 7(f), respectively, clearly show the robustness to the radii deformation. Note that the maximum disorder we consider here is restricted by the structural integrity, which is changeable depending on the design of the band structure. With the ability of being robust to disorders, our work shows great potentials in practical applications.

V. CONCLUSION

In conclusion, we study the non-Hermitian characteristics of coupled topologically protected edge states with a one-dimensional heterogeneous acoustic crystal. The non-Hermitian modulations are done by introducing different passive local sound dissipations. It is found that introducing and increasing the loss can drive the system to reach the exceptional point, where the coupled modes merge in the real spectrum while bifurcating in the imaginary spectrum. A series of asymmetric scattering phenomena are observed both numerically and experimentally, which are subsequently proved to be robust to the geometric imperfections such as position disorder and radii deformation. These intriguing properties are full of practical significance and have potential application in the field of sound insulation since unidirectional reflection and absorption can be a flexible approach to manipulating sound on demand. As the proposed model is generic to the wave physics, our work may provide a flexible route to study the non-Hermitian properties of the topological insulators in different wave systems such as photonics and mechanics.

ACKNOWLEDGMENTS

This work is supported by National Natural Science Foundation of China (Grants No. 11774297, No. 11704284) and General Research Fund (GRF) scheme of Research Grants Council of Hong Kong (Grant No. PolyU 152119/18E).

APPENDIX A: SIMULATION AND EXPERIMENT RESULTS ON THE EMERGENCE OF THE COUPLED TESS

We measure the transmission spectra (black triangle) for S1, S2 and the sandwich stacked structure, respectively, as displayed in Fig. 8. The simulation results (red circle) that consider the thermoviscous effect are also obtained for a comparison. Apparently, there is a deep bandgap around 1780 Hz for both S1 [Fig. 8(a)] and S2 [Fig. 8(b)]. However, since the topological properties of these two bandgaps are different, the TESs can be excited at the interface between them, which also lead to the appearance of

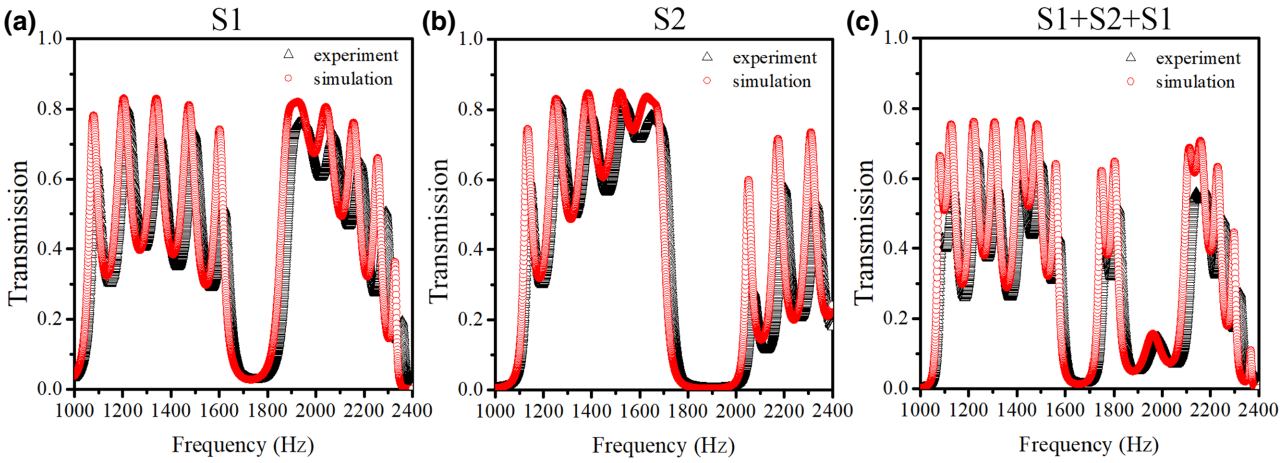

FIG. 8. Transmission spectra for (a) S1 contains nine units; (b) S2 contains nine units; (c) the combination of S1 + S2 + S1, and each part has three units. The red circle indicates the simulation results and the black triangle indicates the measured results.

two peaks in the overlapped bandgap for S1 + S2 + S1 [Fig. 8(c)].

APPENDIX B: EXPERIMENTAL DETAILS

The sample with a total length being 162 cm is divided into three parts to be fabricated with the three-dimensional-printing technology. The polyester fibers are chosen as the sound-absorbing materials to be placed at interfaces of different parts to introduce the loss modulation. The SAMs are placed against the wall of the waveguide, as shown in Fig. 9. The width of SAMs is fixed to 5 cm, while their length and thickness are tuned to induce different levels of loss. The SAM cannot be linked to δ quantitatively, but they have the relation of positive correlation.

During the measurement, the sample is connected to a commercial impedance tube (Brüel & Kjær type-4206T) and four 1/4 condenser microphones (Brüel & Kjær type-4187) are employed at the designed position to detect the amplitudes of sound signals and phase the local field. Then the detected signals are sent to the data-acquisition board for further calculations. The source signal is generated by the computer and boosted by the power amplifier (Brüel & Kjær) before being sent to the loudspeaker.

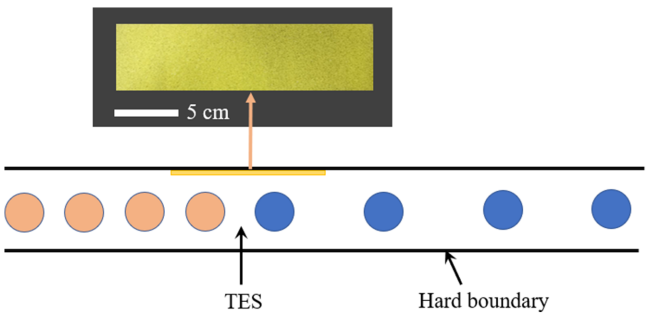

FIG. 9. Implementation of the sound-absorbing materials.

[1] M. Z. Hasan and C. L. Kane, Colloquium: Topological insulators, Rev. Mod. Phys. **82**, 3045 (2010).
[2] M. Konig, S. Wiedmann, C. Brune, A. Roth, H. Buhmann, L. W. Molenkamp, X. L. Qi, and S. C. Zhang, Quantum spin hall insulator state in HgTe quantum wells, Science **318**, 766 (2007).
[3] X. Wan, A. M. Turner, A. Vishwanath, and S. Y. Savrasov, Topological semimetal and Fermi-arc surface states in the electronic structure of pyrochlore iridates, Phys. Rev. B **83**, 205101 (2011).
[4] S. Murakami, N. Nagaosa, and S. C. Zhang, Dissipationless quantum spin current at room temperature, Science **301**, 1348 (2003).
[5] Z. Yang, F. Gao, X. Shi, X. Lin, Z. Gao, Y. Chong, and B. Zhang, Topological Acoustics, Phys. Rev. Lett. **114**, 114301 (2015).
[6] F. Zangeneh-Nejad and R. Fleury, Topological Fano Resonances, Phys. Rev. Lett. **122**, 014301 (2019).
[7] X. Li, Y. Meng, X. Wu, S. Yan, Y. Huang, S. Wang, and W. Wen, Su-Schrieffer-Heeger model inspired acoustic interface states and edge states, Appl. Phys. Lett. **113**, 203501 (2018).
[8] Y. G. Peng, C. Z. Qin, D. G. Zhao, Y. X. Shen, X. Y. Xu, M. Bao, H. Jia, and X. F. Zhu, Experimental demonstration of anomalous Floquet topological insulator for sound, Nat. Commun. **7**, 13368 (2016).
[9] X. Zhang, H.-X. Wang, Z.-K. Lin, Y. Tian, B. Xie, M.-H. Lu, Y.-F. Chen, and J.-H. Jiang, Second-order topology and multidimensional topological transitions in sonic crystals, Nat. Phys. **15**, 582 (2019).
[10] G. Ma, M. Xiao, and C. T. Chan, Topological phases in acoustic and mechanical systems, Nat. Rev. Phys. **1**, 281 (2019).

[11] Y. Qi, C. Qiu, M. Xiao, H. He, M. Ke, and Z. Liu, Acoustic Realization of Quadrupole Topological Insulators, Phys. Rev. Lett. **124**, 206601 (2020).
[12] H. Xue, Y. Ge, H. X. Sun, Q. Wang, D. Jia, Y. J. Guan, S. Q. Yuan, Y. Chong, and B. Zhang, Observation of an acoustic octupole topological insulator, Nat. Commun. **11**, 2442 (2020).
[13] X. Ni, M. Li, M. Weiner, A. Alu, and A. B. Khanikaev, Demonstration of a quantized acoustic octupole topological insulator, Nat. Commun. **11**, 2108 (2020).
[14] J. Lu, C. Qiu, L. Ye, X. Fan, M. Ke, F. Zhang, and Z. Liu, Observation of topological valley transport of sound in sonic crystals, Nat. Phys. **13**, 369 (2016).
[15] H. Xue, Y. Yang, F. Gao, Y. Chong, and B. Zhang, Acoustic higher-order topological insulator on a kagome lattice, Nat. Mater. **18**, 108 (2019).
[16] H. Xue, Y. Yang, G. Liu, F. Gao, Y. Chong, and B. Zhang, Realization of an Acoustic Third-Order Topological Insulator, Phys. Rev. Lett. **122**, 244301 (2019).
[17] F. Zangeneh-Nejad and R. Fleury, Topological analog signal processing, Nat. Commun. **10**, 2058 (2019).
[18] F. Zangeneh-Nejad and R. Fleury, Disorder-Induced signal filtering with topological metamaterials, Adv. Mater. **32**, e2001034 (2020).
[19] H. He, C. Qiu, L. Ye, X. Cai, X. Fan, M. Ke, F. Zhang, and Z. Liu, Topological negative refraction of surface acoustic waves in a Weyl phononic crystal, Nature **560**, 61 (2018).
[20] Z. Zhang, Y. Tian, Y. Cheng, Q. Wei, X. Liu, and J. Christensen, Topological Acoustic Delay Line, Phys. Rev. Appl. **9**, 034032 (2018).
[21] L. Feng, R. El-Ganainy, and L. Ge, Non-Hermitian photonics based on parity–time symmetry, Nat. Photonics **11**, 752 (2017).
[22] R. El-Ganainy, K. G. Makris, M. Khajavikhan, Z. H. Musslimani, S. Rotter, and D. N. Christodoulides, Non-Hermitian physics and PT symmetry, Nat. Phys. **14**, 11 (2018).
[23] M. A. Miri and A. Alu, Exceptional points in optics and photonics, Science **363**, eaar7709 (2019).
[24] V. Achilleos, G. Theocharis, O. Richoux, and V. Pagneux, Non-Hermitian acoustic metamaterials: Role of exceptional points in sound absorption, Phys. Rev. B **95**, 144303 (2017).
[25] S. Weidemann, M. Kremer, T. Helbig, T. Hofmann, A. Stegmaier, M. Greiter, R. Thomale, and A. Szameit, Topological funneling of light, Science **368**, 311 (2020).
[26] R. Fleury, D. Sounas, and A. Alu, An invisible acoustic sensor based on parity-time symmetry, Nat. Commun. **6**, 5905 (2015).
[27] X. Zhu, H. Ramezani, C. Shi, J. Zhu, and X. Zhang, PT-Symmetric Acoustics, Phys. Rev. X **4**, 031042 (2014).
[28] Y. D. Chong, L. Ge, and A. D. Stone, PT-symmetry Breaking and Laser-Absorber Modes in Optical Scattering Systems, Phys. Rev. Lett. **106**, 093902 (2011).
[29] L. Ge, Y. D. Chong, and A. D. Stone, Conservation relations and anisotropic transmission resonances in one-dimensionalPT-symmetric photonic heterostructures, Phys. Rev. A **85**, 023802 (2012).
[30] R. Fleury, D. L. Sounas, and A. Alu, Parity-Time symmetry in acoustics: Theory, devices, and potential applications, IEEE J. Sel. Top. Quantum Electron **22**, 121 (2016).
[31] S. K. Ozdemir, S. Rotter, F. Nori, and L. Yang, Parity-time symmetry and exceptional points in photonics, Nat. Mater. **18**, 783 (2019).
[32] W. Zhu, X. Fang, D. Li, Y. Sun, Y. Li, Y. Jing, and H. Chen, Simultaneous Observation of a Topological Edge State and Exceptional Point in an Open and Non-Hermitian Acoustic System, Phys. Rev. Lett. **121**, 124501 (2018).
[33] K. Zhu, Y. Sun, J. Ren, and H. Chen, Loss revives bistable state near the exceptional point in a non-Hermitian microwave photonic meta-molecule, New J. Phys. **19**, 063043 (2017).
[34] T. Liu, X. Zhu, F. Chen, S. Liang, and J. Zhu, Unidirectional Wave Vector Manipulation in Two-Dimensional Space with an All Passive Acoustic Parity-Time-Symmetric Metamaterials Crystal, Phys. Rev. Lett. **120**, 124502 (2018).
[35] A. Merkel, V. Romero-García, J.-P. Groby, J. Li, and J. Christensen, Unidirectional zero sonic reflection in passive PT-symmetric Willis media, Phys. Rev. B **98**, 201102(R) (2018).
[36] H. Z. Chen, T. Liu, H. Y. Luan, R. J. Liu, X. Y. Wang, X. F. Zhu, Y. B. Li, Z. M. Gu, S. J. Liang, H. Gao, L. Lu, L. Ge, S. Zhang, J. Zhu, and R. M. Ma, Revealing the missing dimension at an exceptional point, Nat. Phys. **16**, 571 (2020).
[37] H. Zhao, X. Qiao, T. Wu, B. Midya, S. Longhi, and L. Feng, Non-Hermitian topological light steering, Science **365**, 1163 (2019).
[38] Z. Zhang, M. Rosendo Lopez, Y. Cheng, X. Liu, and J. Christensen, Non-Hermitian Sonic Second-Order Topological Insulator, Phys. Rev. Lett. **122**, 195501 (2019).
[39] M. Wang, L. Ye, J. Christensen, and Z. Liu, Valley Physics in Non-Hermitian Artificial Acoustic Boron Nitride, Phys. Rev. Lett. **120**, 246601 (2018).
[40] C. Shen, J. F. Li, X. Y. Peng, and S. A. Cummer, Synthetic exceptional points and unidirectional zero reflection in non-Hermitian acoustic systems, Phys. Rev. Mater. **2**, 125203 (2018).
[41] H. Gao, H. Xue, Q. Wang, Z. Gu, T. Liu, J. Zhu, and B. Zhang, Observation of topological edge states induced solely by non-Hermiticity in an acoustic crystal, Phys. Rev. B **101**, 180303(R) (2020).
[42] W. Song, W. Sun, C. Chen, Q. Song, S. Xiao, S. Zhu, and T. Li, Breakup and Recovery of Topological Zero Modes in Finite Non-Hermitian Optical Lattices, Phys. Rev. Lett. **123**, 165701 (2019).
[43] M. Xiao, G. Ma, Z. Yang, P. Sheng, Z. Q. Zhang, and C. T. Chan, Geometric phase and band inversion in periodic acoustic systems, Nat. Phys. **11**, 240 (2015).
[44] Y. Zhu and L. Zhu, Accessing the exceptional points in coupled fabry–perot resonators through hybrid integration, ACS Photonics **5**, 4920 (2018).